

Multidisciplinary inferences on a newly recognized active east-dipping extensional system in Central Italy

G. Lavecchia¹, G. M. Adinolfi¹, R. de Nardis^{1,3}, F. Ferrarini¹, D. Cirillo¹,
F. Brozzetti¹, R. De Matteis², G. Festa⁴ and A. Zollo⁴

¹CRUST, DiSPUTer, Università "G. d'Annunzio", Chieti Scalo, Italy

²Dipartimento di Scienze e Tecnologie, Università degli Studi del Sannio, Benevento, Italy

³Dipartimento della Protezione Civile, Rome, Italy

⁴, Dipartimento di Fisica "Ettore Pancini", Università di Napoli Federico II, Naples, Italy

Contents of this file

[Figs.S1 to S8](#)

Introduction

This supplement contains supporting Figures cited in the main document, with extensive captions. It is aimed at giving additional information on:

- the computed TDMT focal mechanism and uncertainty analysis of the largest aftershock of L'Aquila 6 April 2009 (M_w 6.3), occurred on 7 April 2009 (M_w 5.4, EQ2) ([Figs. S1 and S2](#));
- the source slip model of EQ2([Fig.S3](#));
- the 3D-model fault building of the Paganica and Ocre fault segments ([Fig. S4](#));
- the extensional tectonic setting of the Sabini-Eastern Simbruini (SES) (central Italy, Latium-Abruzzo political boundary), with a new geological sketch of the area ([Fig. S5](#)), plus new structural data and a seismic lines interpretation ([Fig.S6](#));
- the analysis of the kinematic compatibility of the EQ2 preferential seismic plane with the inverted seismological stress tensor ([Fig.S7](#));
- a schematic geometric explanation for differential amount of displacement on the LAED (Latium-Abruzzi Extensional Detachment) at different structural levels ([Fig. S8](#)).

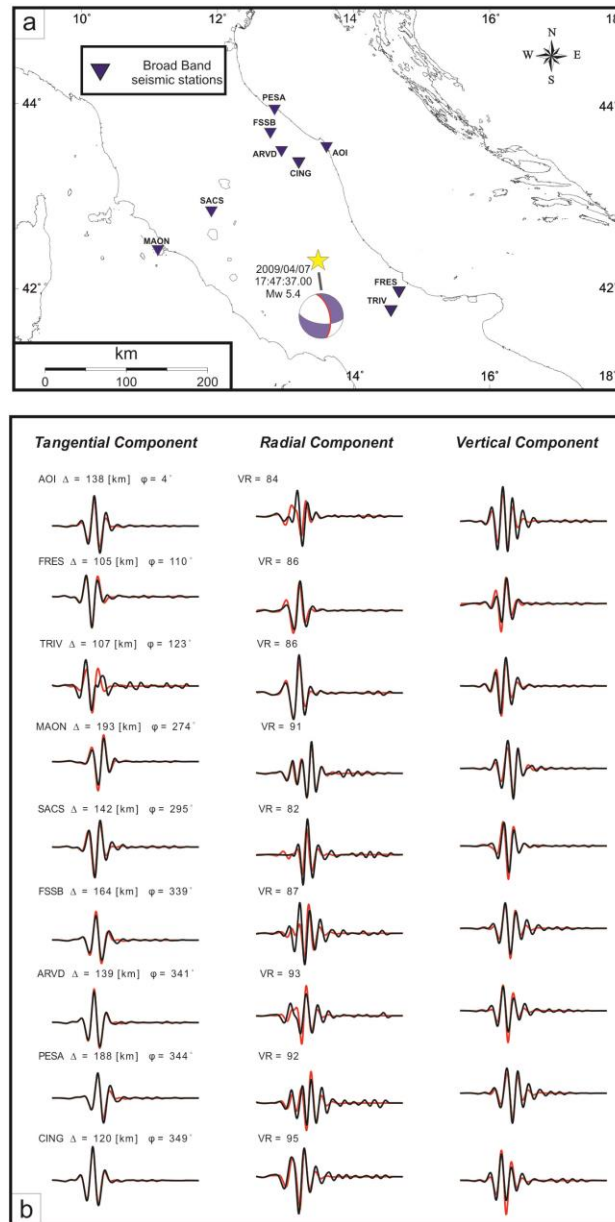


Fig. S1 - a) Centralized National Seismic Network (RSNC) broad-band seismic stations (triangles) used in this study for the TDMT inversion. b) Displacement waveform fit between observed (black lines) and synthetic (red lines) data of the TDMT solution (Dreger and Helmberger, 1993; Dreger, 2003) obtained for EQ2. The seismograms are sorted by increasing source-to-station azimuth (ϕ), epicentral distance (Δ) and variance reduction (VR) are also reported. We used broadband velocity waveforms that were recorded at RSNC between 100km and 400km from the earthquake epicenter to consider records with good signal-to-noise ratios and to avoid the use of saturated waveforms. The Green's functions were computed with the frequency–wave number integration method (Saikia, 1994) in the 1-D regional velocity model that was proposed by Hermann et al. (2011). After fixing the depth and the location of the earthquake, we inverted data from 9 stations and obtained a solution with a variance reduction of $\sim 89\%$ and a percentage of double couple (DC) of $\sim 91\%$.

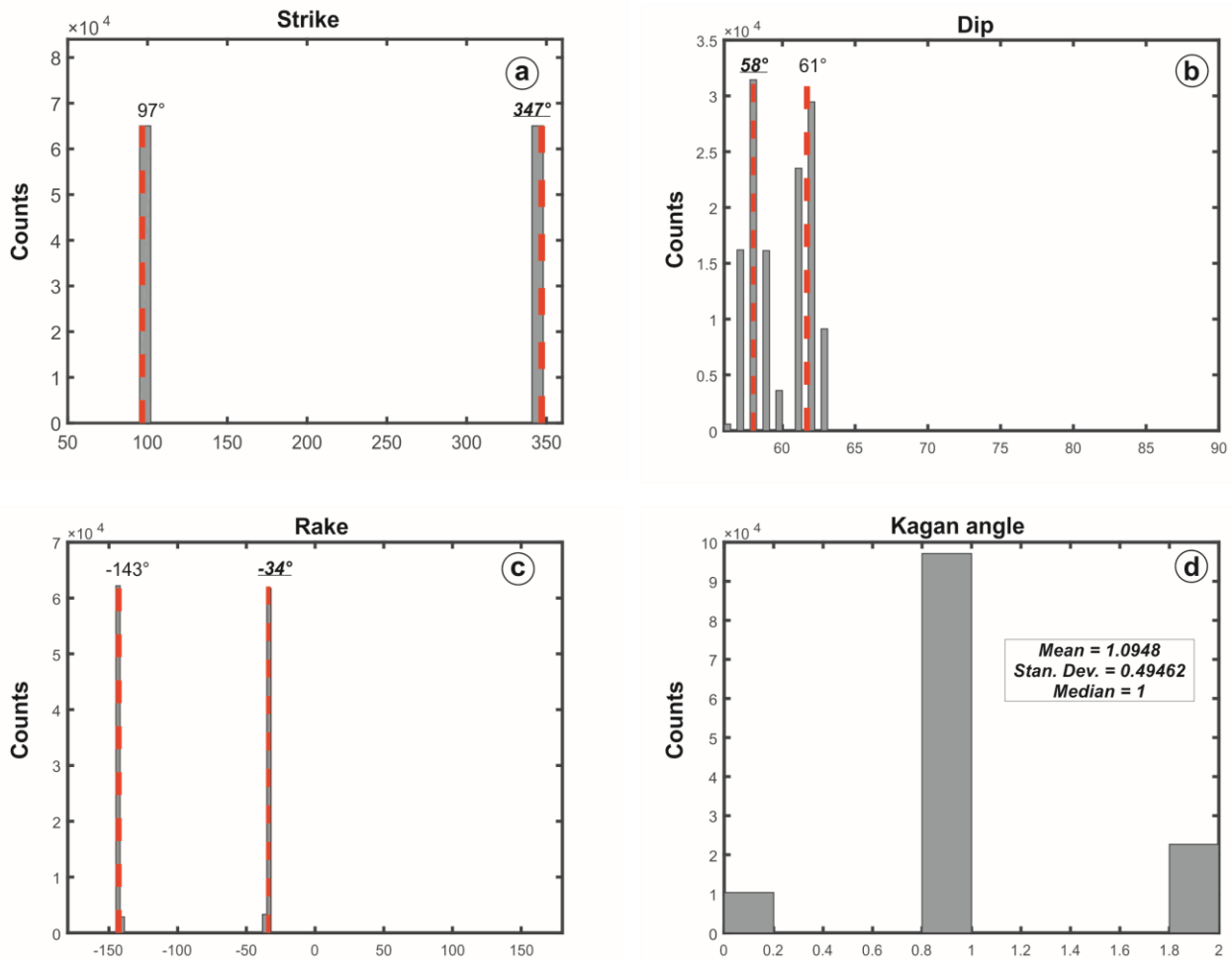


Fig. S2 - Uncertainty assessment of the source angles and Kagan angle of the calculated TDMT solution (Tab. 1 of the main document). The uncertainty analysis was performed by calculating the theoretical error ellipsoid for a fixed source position and time as proposed by Sokos and Zahradník (2013) with ISOLA software (Sokos and Zahradník, 2008). The source-station configuration, frequency range, and the crustal model define the ellipsoid shape and orientation, while the absolute size of the error ellipsoid is determined by the variance of data. In each panel, the nodal planes are indicated with red dashed lines and are derived from the moment tensor solution calculated in this study. The grey histograms represent the potential and acceptable solutions, function of the data variance. The angle values associated with the constrained seismic preferential plane are reported in underlined bold italic. The uncertainty values are considerably small indicating a constrained focal mechanism solution. Referring to preferential seismic plane, the strike value varies between 347° and 344° (a); the dip value centered on 58° varies in a range of 4° (b) while the rake (-34°) varies mainly between -32° and -34° (c). Moreover, the Kagan angle, that is the angle between acceptable solutions compared with the optimal solution, show values whose mean is about 1° with a standard deviation of 0.5 (d). This additional parameter underlines the low uncertainty of the focal mechanism solution.

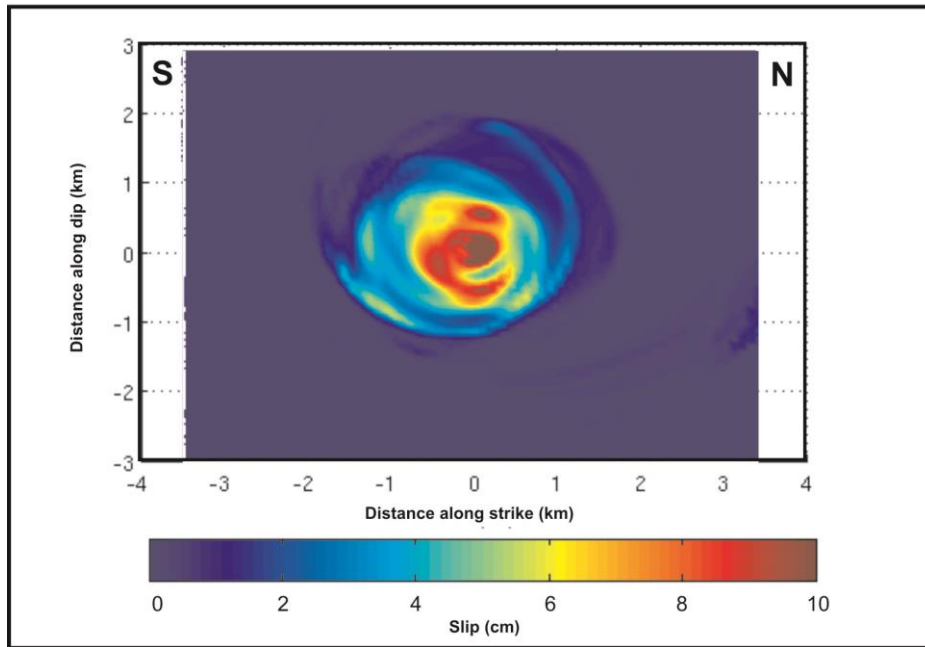


Fig. S3 - a) EQ2 slip map obtained by isochrone back-projection computed with a rupture velocity of 1.8 km/s. The ASTFs shapes discriminate the ENE-dipping plane of the computed TDMT focal mechanism (Fig. 2a in the main document) as the one for which the misfit function is minimum (Fig.2c in the main document). After testing different rupture velocities, we selected the final kinematic model that minimizes the L1-norm between the synthetic and observed ASTFs (Fig.2b in the main document). The fault geometry was fixed at the solution that is derived from the computed focal mechanism (ENE-dipping plane). We adopted the deconvolution technique that was proposed by Vallée (2004). The deconvolution was performed at 15 stations (Fig. 2a in the main document) for the direct S wave in the frequency range of 0.01–2Hz based on the limits that were imposed by the expected corner frequency of the master event and the stability of the S-wave polarization.

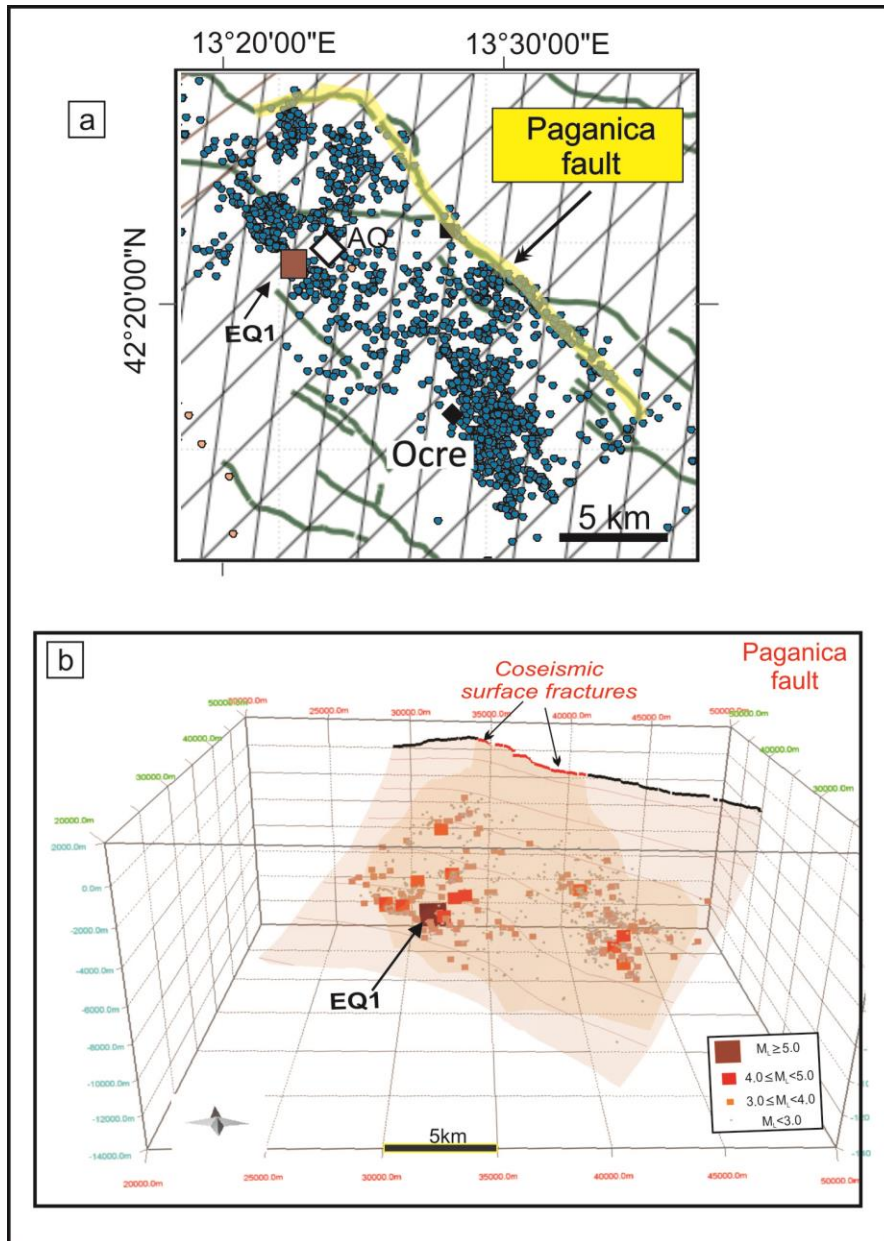


Fig. S4- a, b) 3D-model building of the Paganica fault segment activated by EQ1 and its aftershock sequences in the time interval from April 6 to September 30, 2009 (dataset from [Chiaraluce et al., 2011](#)). To reconstruct the 3D surfaces we adopted a semi-automatic procedure through the use of the Midland Valley MOVE software (vers. 2016). First, we traced closely-spaced (1.25 km semi-width) and differently oriented set of sections across the epicentral area, in the MOVE georeferenced frame. Second, we drew the fault trace connecting the aftershock volume and the surface fault in the MOVE section view window. Third, we used the Delaunay Triangulation function to build the fault surfaces. The extent of this seismogenic patch activated by the 6 April main shock and by its aftershock sequence with respect to the overall Paganica surface is highlighted in [Fig. S4b](#).

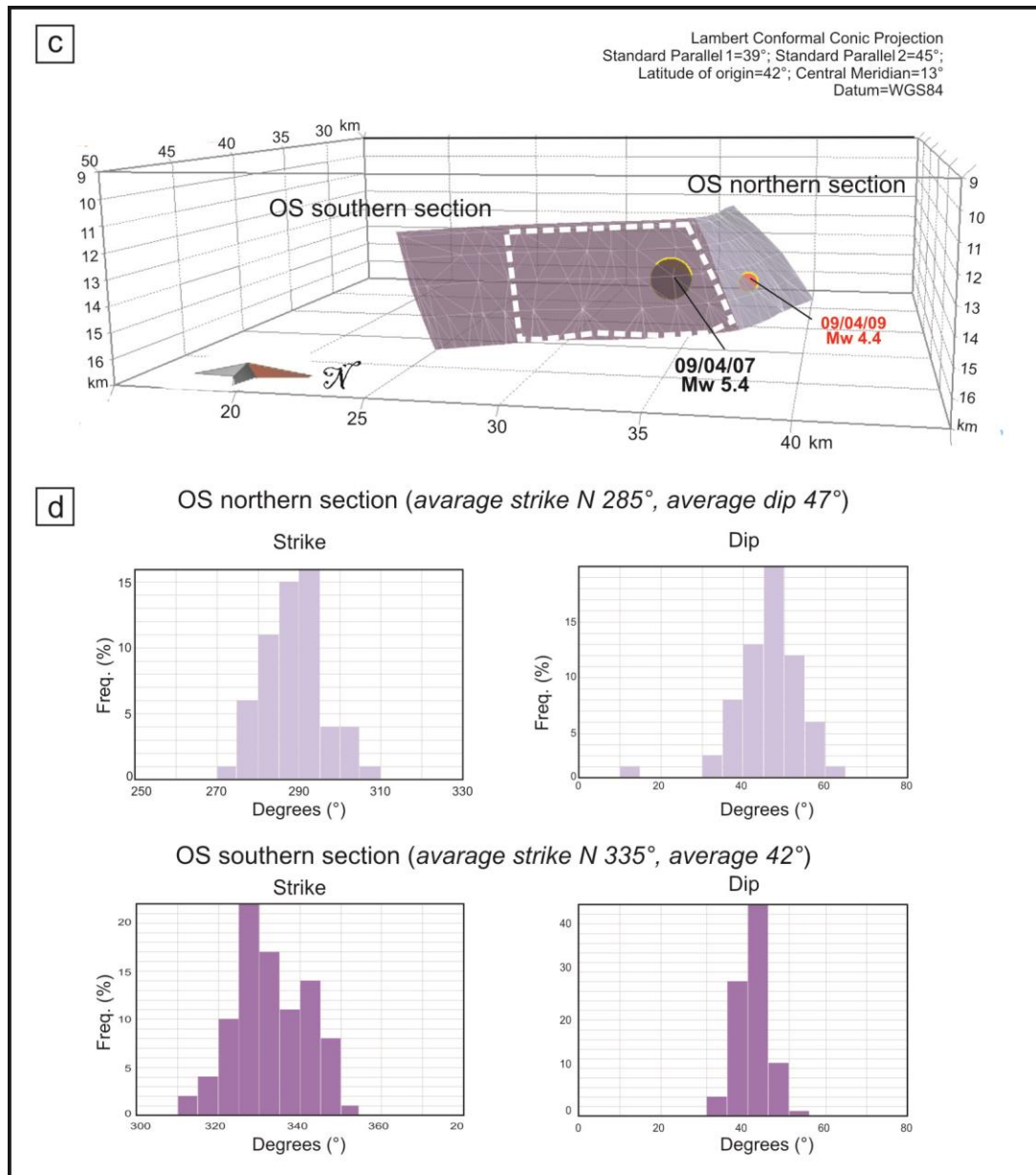


Fig. S4 - c, d) 3D-model building of the Ocre Segment (OS) activated by EQ2 and by the other deep events (depth >11 km) of L'Aquila 2009 sequence (dataset from Chiaraluce *et al.*, 2011). (c) Triangulated meshes of the OS surface reconstructed according to the same work-flow adopted for the Paganica fault in Fig. S4b. The white dashed line represents a schematic representation of the EQ2 (M_w 5.4) rupture area calculated according to scale law (about 6x7 km from Wells and Coppersmith, 1994). (d) Histograms of the strike and dip of the OS triangulated surfaces that show the OS along-strike and along-dip variability.

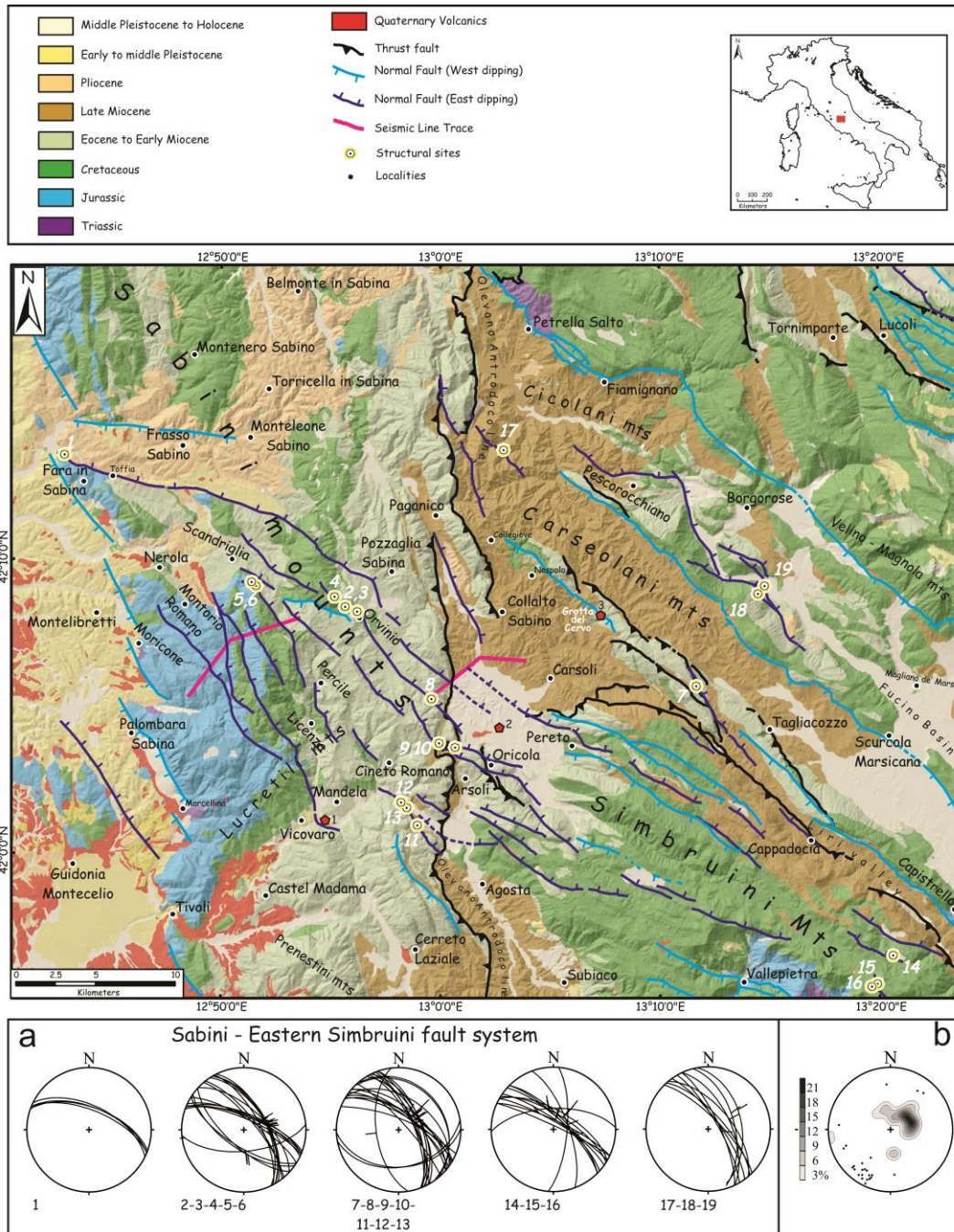


Fig. S5 - Geological map of the Sabini-Eastern Simbruini (SES) and of the Carseolani Mts. area, simplified from the Carta Geologica d'Italia, 1:100,000 scale, sheets 144-145-150-151 (Servizio Geologico d'Italia at http://193.206.192.231/carta_geologica_italia/default.htm) and redrawn on a GIS-platform with original field data from the authors. The map is overlain on a 20m digital elevation model. The structural sites surveyed along the SES normal faults are indicated as yellow dots, and numbered from 1 to 19; the corresponding fault/slip data are represented in a number of stereographic plots (Schmidt net, lower hemisphere) both as a) cyclographic trace/lineation and b) poles to major normal faults and contouring of the associated slip vectors.

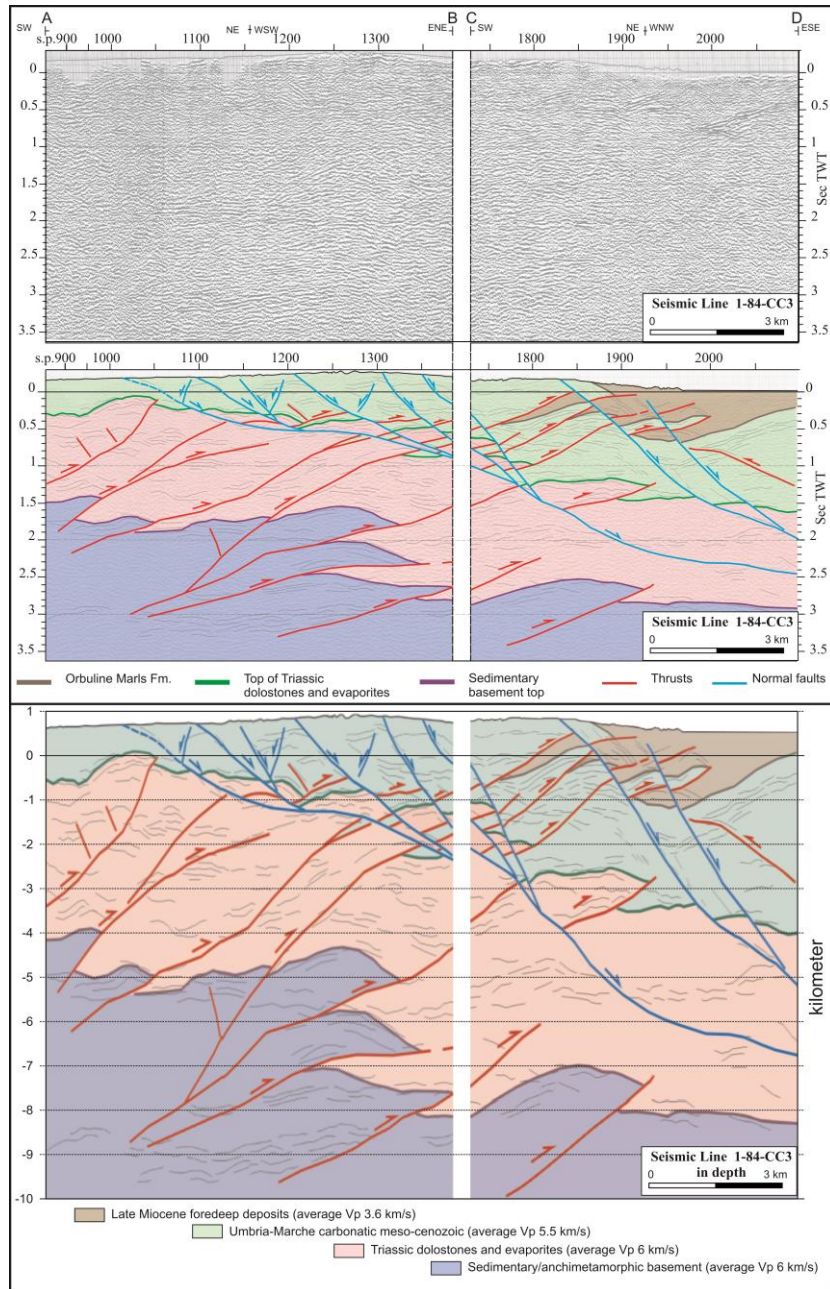


Fig. S6 - Two portions of the commercial seismic line 1-84-CC3 (VIDEPI Project, 2016 at <http://unmig.mise.gov.it/deposito/videpi/allegati/1214.pdf>) extending in an average SW-NE direction across the Sabini-Eastern Simbruini (SES) extensional system (traces in Fig. S5) with corresponding line drawing and geological interpretation of the main reflectors and seismic facies. In spite of the general poor quality of the line, some closely spaced and relatively continuous packages of reflections, separated by areas with low-continuity signals, can be detected and traced along the entire develop of the section. Taking into account the outcropping stratigraphic units and fault planes (Fig. S5), the average stratigraphic thickness given in the literature (Patacca et al., 2008; Cosentino et al., 2010) and the corresponding seismic and mechanical stratigraphy (Di Luzio et al., 2009 and references therein), these reflectors can be referred to the tops and the stratigraphic units reported in the legend

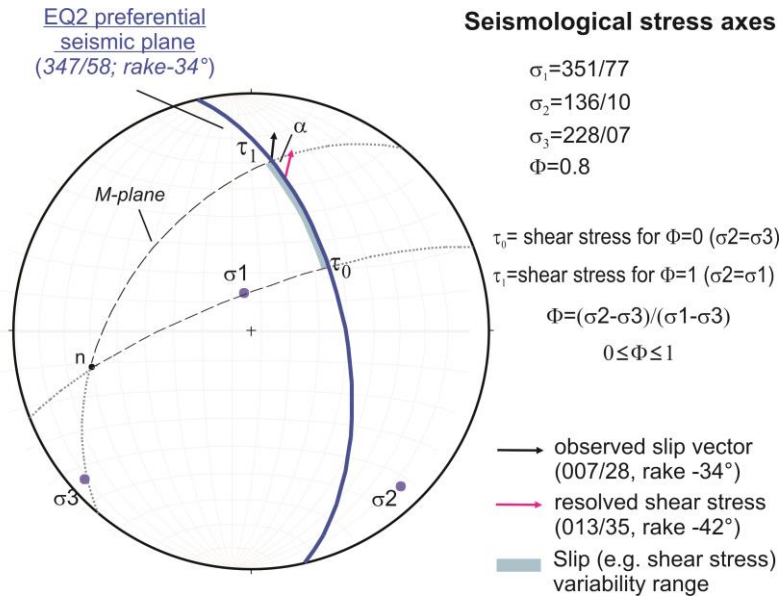


Fig.S7. Slip vector variability range for the preferential fault plane of the EQ2 focal mechanism (Tab.1), in the L'Aquila 2009 computed extensional stress regime (Tab.2), as function of the stress ratio Φ (after Angelier, 1994). Key: EQ2 preferential seismic plane as in Fig.2a; n= pole to the EQ2 preferential seismic plane; $\sigma_1, \sigma_2, \sigma_3$ = principal stress axes as in Tab.2; α =misfit angle between the observed and the optimized slip vector on the EQ2 preferential seismic plane; M-Plane = Movement plane which contains the pole to the fault plane and the slip direction. The extreme positions of shear stresses, e.g. τ_0 (for $\Phi=0$, when $\sigma_2=\sigma_3$) and τ_1 (for $\Phi=1$, when $\sigma_2=\sigma_1$), define the slip variability range (as Φ increases from 0 to 1), the slip vector being assumed to be parallel to shear stress. In our specific case, both the EQ2 measured slip vector as well as the EQ2 resolved shear stress fall within the range of slip variability. Coherently with the calculated stress ratio value ($\Phi=0.8$) (Tab.2), they both place near the τ_1 value. The reconstructed picture shows as, in spite of its relevant left-lateral strike-slip component, the EQ2 preferential seismic plane is kinematically compatible with the overall L'Aquila 2009 extensional tensor.

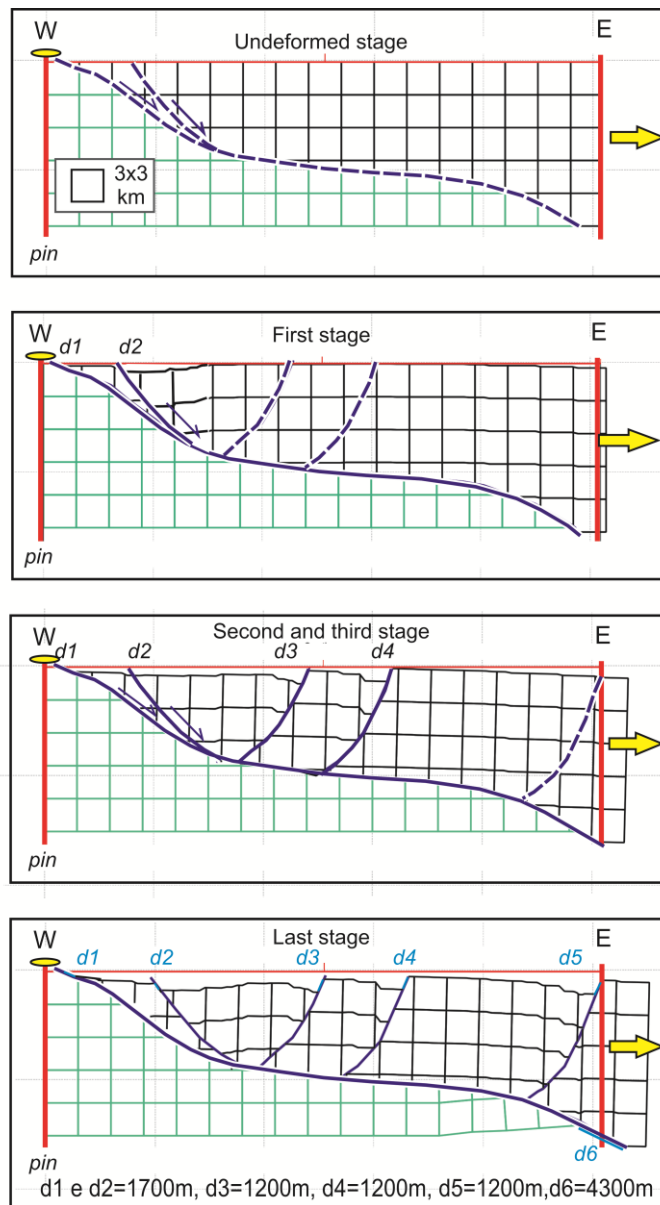


Fig. S8 - Sequential steps of offset accommodation across a schematic section that in its final stage recalls the LAED structural style, e.g. an east-dipping detachment with a double-ramp geometry coupled with antithetic west-dipping high-angle faults. A simple forward model was built with Move software (Midland valley, 2016), assuming that the hanging-wall faults progressively grew eastward. The diagram helps to highlight the different partitioning of net extension at surface and at depth. In fact, at surface the net displacement of the final stage section is accommodated prevalingly by high-angle west-dipping faults (d_3 , d_4 , d_5) and subordinately by the moderately east-dipping ones (d_1 , d_2). At depth, conversely, almost all the displacement (d_6) results to be achieved along the basal extensional detachment.